

## Phonon anomalies associated with spin reorientation in the kagome ferromagnet Fe<sub>3</sub>Sn<sub>2</sub>

Ge He, Leander Peis, Ramona Stumberger, Lilian Prodan, Vladimir Tsurkan, Nico Unglert, Liviu Chioncel, István Kézsmárki, Rudi Hackl

### Angaben zur Veröffentlichung / Publication details:

He, Ge, Leander Peis, Ramona Stumberger, Lilian Prodan, Vladimir Tsurkan, Nico Unglert, Liviu Chioncel, István Kézsmárki, and Rudi Hackl. 2022. "Phonon anomalies associated with spin reorientation in the kagome ferromagnet Fe<sub>3</sub>Sn<sub>2</sub>." *physica status solidi (b)* 259 (5): 2100169. <https://doi.org/10.1002/pssb.202100169>.

# Phonon Anomalies Associated with Spin Reorientation in the Kagome Ferromagnet $\text{Fe}_3\text{Sn}_2$

Ge He, Leander Peis, Ramona Stumberger, Lilian Prodan, Vladimir Tsurkan, Nico Unglert, Liviu Chioncel, István Kézsmárki, and Rudi Hackl\*

Polarization- and temperature-dependent Raman data along with theoretical simulations are presented for the Kagome ferromagnet  $\text{Fe}_3\text{Sn}_2$ . Eight out of nine expected phonon modes are identified. The experimental energies compare well with those from the simulations. The analysis of the line widths indicates relatively strong phonon–phonon coupling in the range 0.1–1. The temperature-dependent frequencies of three  $A_{1g}$  modes show weak anomalies at  $\approx 100$  K. In contrast, the linewidths of all phonon modes follow the conventional exponential broadening up to room temperature except for the softest  $A_{1g}$  mode, whose width exhibits a kink close to 100 K and becomes nearly constant for  $T > 100$  K. These features are indicative of a spin reorientation taking place in the temperature range above 100 K, which might arise from spin–phonon coupling. The low-energy part of the electronic continuum in  $E_g$  symmetry depends strongly on temperature. The possible reasons include particle–hole excitation tracking the resistivity, a spin-dependent gap, or spin fluctuations.

## 1. Introduction

Materials with novel properties and functionalities have intriguing scientific and applied perspectives. In particular magnets with exotic ground states continue to attract attention because the properties may be tailored via the lattice and/or the electronic band structure.  $\text{Fe}_3\text{Sn}_2$  is a layered Kagome ferromagnet with a very high Curie temperature  $T_C = 670$  K. The Fe–Sn bilayers are separated by Sn monolayers,<sup>[1–4]</sup> as shown in **Figure 1a**. Due to its out-of-plane anisotropy<sup>[2,3]</sup> with the magnetic easy axis perpendicular to the Kagome layers, magnetic stripes and a variety of magnetic bubbles have been observed in thin lamellae using Lorentz transmission electron microscopy.<sup>[5–8]</sup>

Because the material possesses inversion symmetry, these mesoscale magnetic textures do not form due to the antisymmetric part of the exchange coupling tensor, i.e., the Dzyaloshinskii–Moriya interaction, but due to a competition between the out-of-plane anisotropy and the magnetic dipole–dipole interaction. The magnetic anisotropy of the system is also linked to the reconstruction of its band structure in a magnetic field: a strong shift of bands close to the Fermi energy was found to be dependent not only on the magnitude but also on the orientation of the magnetic field.<sup>[9]</sup> Moreover, indications of a temperature-driven spin reorientation, from out-of-plane at high temperatures toward in-plane at low temperatures, have been found earlier in Mössbauer,<sup>[2,3]</sup> X-ray,<sup>[4]</sup> and transport studies.<sup>[10]</sup> Optical absorption experiments<sup>[11]</sup> reveal an additional feature in the 10 meV range below 150 K and associate it with this spin reorientation. Similarly, transport and magnetization experiments (performed on our own samples and plotted in **Figure 1b,c**) show a crossover temperature close to 100 K and will be discussed in detail in Section 2.1.


There are various other effects in a planar hexagonal lattice, such as massless Dirac fermions. As opposed to graphene, the tips of the cones typically intersect below the Fermi energy  $E_F$  and may become massive in the presence of spin–orbit coupling (SOC).<sup>[9,12]</sup> Recently, the existence of flat bands at  $\approx 200$  meV below  $E_F$  in confined regions of the Brillouin zone was associated with magnetic ordering in  $\text{Fe}_3\text{Sn}_2$ .<sup>[13]</sup> These observations and suggestions are among the main motivations for this work, focusing on spin reorientation and band reconstruction phenomena in  $\text{Fe}_3\text{Sn}_2$  and its consequences for the

G. He, L. Peis, R. Stumberger, R. Hackl  
Walther Meissner Institut  
Bayerische Akademie der Wissenschaften  
85748 Garching, Germany  
E-mail: hackl@tum.de

R. Stumberger, R. Hackl  
Fakultät für Physik  
Technische Universität München  
85748 Garching, Germany

L. Prodan, V. Tsurkan, L. Chioncel, I. Kézsmárki  
Experimentalphysik V  
Institut für Physik  
Universität Augsburg  
Universitätsstrasse 1 (Physik Süd), 86159 Augsburg, Germany

N. Unglert  
Theoretische Physik III  
Institut für Physik  
Universität Augsburg  
Universitätsstrasse 1 (Physik Süd), 86159 Augsburg, Germany

 The ORCID identification number(s) for the author(s) of this article can be found under <https://doi.org/10.1002/pssb.202100169>.

© 2021 The Authors. physica status solidi (b) basic solid state physics published by Wiley-VCH GmbH. This is an open access article under the terms of the Creative Commons Attribution License, which permits use, distribution and reproduction in any medium, provided the original work is properly cited.

DOI: 10.1002/pssb.202100169

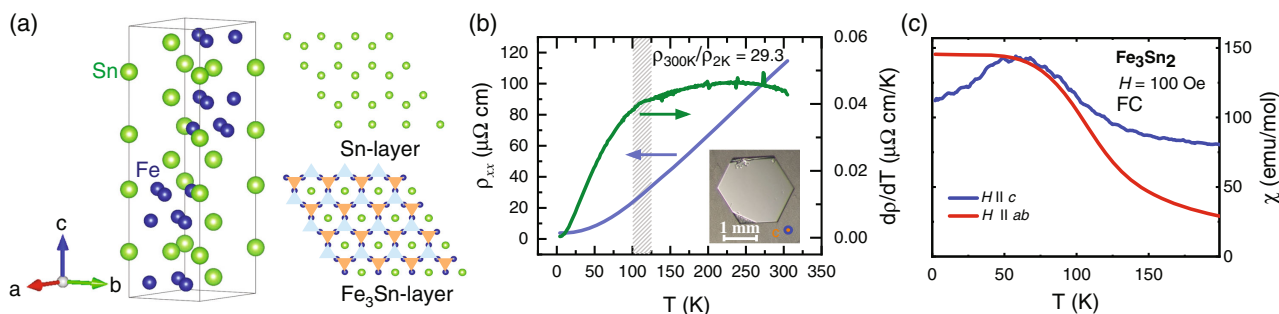


**Figure 1.** Properties of Fe<sub>3</sub>Sn<sub>2</sub>. a) Crystal structure (left). The crystals consist of hexagonal Sn layers sandwiched between Kagome Fe<sub>3</sub>Sn double layers (right). b) Resistivity  $\rho(T)$  of Fe<sub>3</sub>Sn<sub>2</sub>.  $\rho(T)$  (blue) was measured on a crystal from the same batch as the sample used here.  $d\rho(T)/dT$  (green, right axis) is nearly constant above 100 K, indicating a linear temperature dependence of  $\rho(T)$ . Below a rather well-defined kink at 100 K, the slope changes rapidly. c) Anisotropic susceptibility  $\chi_i(T)$  for field orientations as indicated. The sample was cooled in an applied field of  $\mu_0 H = 0.01$  T.  $\chi_{ab}(T)$  increases monotonously and almost saturates below 50 K.  $\chi_c(T)$  has a maximum between 50 and 100 K.

lattice dynamics and charge response, both probed by Raman spectroscopy.

Spin textures usually entail a huge anomalous Hall effect (AHE) being associated with the Berry phase the electrons pick up upon moving across a magnetic background.<sup>[14]</sup> Thus Fe<sub>3</sub>Sn<sub>2</sub> has similarities with, e.g., MnSi<sup>[15]</sup> and various other compounds. The origin, however, of the rather complex itinerant ferromagnetism with a high  $T_C$  and a spin reorientation at some 100 K is elusive. The most popular approaches are based on the Hubbard model and either favor flat-band ferromagnetism<sup>[16–18]</sup> or a trade-off between potential and kinetic energy.<sup>[13,19,20]</sup> The latter case is reminiscent of the magnetism in Fe(Se,Te), where itinerant and nearly localized spins seem to cooperate as well.<sup>[21–23]</sup>

It is unlikely that the magnetism in Fe<sub>3</sub>Sn<sub>2</sub> can be observed directly in a similar fashion as in FeSe because the two-magnon excitations typical for antiferromagnets<sup>[24]</sup> do not exist here. However, indirect signatures of spin order, the spin reorientation, or the interaction between spin, lattice, and electrons may be expected, in particular gaps between flatbands such as in the optical experiments<sup>[11]</sup> or phonon renormalization effects as in MnSi.<sup>[25]</sup> In this, to our knowledge first, Raman study of the topological material Fe<sub>3</sub>Sn<sub>2</sub>, we start with analyzing the phonons.

## 2. Experimental Section

### 2.1. Samples

Fe<sub>3</sub>Sn<sub>2</sub> single crystals were grown by the chemical transport reaction method. As starting material, a presynthesized polycrystalline powder prepared by solid state reaction from the high-purity elements Fe (99.99%) and Sn (99.995%) was used. Iodine was used as the transport agent. The growth was performed in SiO<sub>2</sub> ampoules in two-zone furnaces at temperatures between 730 and 680 K. After 4–6 weeks of transport, the single crystals, having a plate-like form with a thickness in the range 20–40  $\mu\text{m}$  along the  $c$ -axis and 3–5 mm in the  $ab$ -plane (see inset of Figure 1b), were found in the hot part of ampoule.

The sample used for the experiments had a residual resistance ratio of  $\text{RRR} = 29.3$  (Figure 1b), indicating high crystalline quality. The derivative of the resistivity,  $d\rho(T)/dT$  (green graph), indicated a qualitative change of the slope at  $\approx 100$  K where all

spins were expected to be finally parallel to the  $ab$  plane. Figure 1c shows the temperature dependences of the in-plane and out-of-plane magnetic susceptibilities,  $\chi_{ab}$  and  $\chi_c$ , respectively. For the analysis of the out-of-plane susceptibility, demagnetization effects had to be taken into account because of the thin-slab geometry of the sample. At high temperatures,  $\chi_c$  is more than three times larger than  $\chi_{ab}$ . Toward 100 K this difference diminishes. Below 100 K  $\chi_c$  starts to decrease and  $\chi_{ab}$  saturates. Consequently, at low temperatures the  $c$ -axis becomes harder than the in-plane direction with  $\chi_{ab}/\chi_c \approx 1.2$  at 2 K. In the same temperature range, where  $\chi_{ab}$  and  $\chi_c$  cross each other, the resistivity shows a kink, as best seen in its temperature derivative in Figure 1b. After witnessing the spin reorientation in magnetic and transport properties, the Raman spectroscopic study of Fe<sub>3</sub>Sn<sub>2</sub>, which is the main subject of this work, is turned to.

### 2.2. Light Scattering

Polarized inelastic light scattering experiments were performed at an excitation wavelength of 575 nm (Coherent GENESIS MX-SLM577-500). The samples were attached to the cold finger of a <sup>4</sup>He flow cryostat. Polarized photons hit the sample at an angle of incidence of 66°, yielding a spot size of  $\approx 50 \times 100 \mu\text{m}^2$ . The polarized scattered photons were collected along the surface normal of the sample and focused on the entrance slit of a double monochromator. The resolution of the spectrometer was set at  $2.8 \text{ cm}^{-1}$ . Polarized photons having the selected energy were recorded with a CCD detector. The number of photons per second is proportional to the Van-Hove function  $S(q \approx 0, \Omega) = \hbar/\pi \{1 + n(\Omega, T)\} \chi''(\Omega, T)$ , where  $n(\Omega, T)$  is the Bose factor and  $\chi''$  is the imaginary part of the Raman response function. The factor  $R$  is the constant of proportionality which absorbs all experimental factors.

For the measurements shown here, only two polarization configurations were used,  $RR$  and  $RL$ , where  $R = 2^{-1/2}(x + iy)$  and  $L = 2^{-1/2}(x - iy)$  for the incoming light (first symbol) inside the sample. An absorbed laser power of  $P_{\text{abs}} = 4.0 \text{ mW}$  independent of the polarization was used.  $P_{\text{abs}}$  induced a heating in the spot region of  $\approx 1\text{--}2 \text{ K mW}^{-1}$ . Here only the holder temperature is indicated. Because (near) backscattering configurations are used, both signs change for the scattered light (second symbol).

The details of the Raman selection rules are discussed later. Due to the symmetric shape of the observed phonon modes and the narrow line width (FWHM),  $\Gamma_L(T) \ll \omega_0(T)$ , where  $\omega_0$  is the resonance energy of the respective mode, their line shapes may be described by temperature-dependent Lorentz functions.

### 2.3. Selection Rules and Simulations

The Raman-active phonon energies and eigenvectors at the  $\Gamma$  point of the Brillouin zone were derived on the basis of the crystal structure using density functional theory (DFT). The symmetry selection rules may be determined from the point group and the atomic positions in the crystal. The space group of  $\text{Fe}_3\text{Sn}_2$  is  $R\bar{3}m$  (No. 166) and belongs to the  $D_{3d}(\bar{3}m)$  point group. The corresponding Raman tensors read

$$A_{1g} = \begin{pmatrix} a & 0 & 0 \\ 0 & a & 0 \\ 0 & 0 & b \end{pmatrix}, \quad (1)$$

$$E_g^{(1)} = \begin{pmatrix} c & 0 & 0 \\ 0 & -c & d \\ 0 & d & 0 \end{pmatrix}, \text{ and} \quad (2)$$

$$E_g^{(2)} = \begin{pmatrix} 0 & -c & -d \\ -c & 0 & 0 \\ -d & 0 & 0 \end{pmatrix}. \quad (3)$$

According to the Wyckoff positions of the Fe (18h) and Sn atoms (6c) in  $\text{Fe}_3\text{Sn}_2$ , there are  $4A_{1g}$  and  $5E_g$  Raman-active phonons. On the basis of the Raman tensors (Equation (1)–(3)) the  $A_{1g}$  and  $E_g$  phonons may be projected separately in the  $RR$  and  $RL$  channel, respectively.

Electronic structure calculations were conducted using DFT and the projector augmented wave (PAW) method as implemented in VASP.<sup>[26–29]</sup> The generalized gradient approximation as parameterized in the Perdew–Burke–Ernzerhof (PBE) functional<sup>[30]</sup> was used to treat exchange and correlation effects. The cutoff for the plane-wave basis was chosen as 680 eV, and the Brillouin zone was sampled with a  $10 \times 10 \times 10$   $\Gamma$ -centered Monkhorst–Pack grid. The  $\text{Fe}_3\text{Sn}_2$  crystal structure reported in Fenner et al.<sup>[4]</sup> was fully relaxed until the forces on all atoms were below  $0.001 \text{ eV } \text{\AA}^{-1}$ .  $\Gamma$ -point phonon calculations were performed using density functional perturbation theory as implemented in VASP. For the symmetry analysis of all phonon modes the Phonopy package<sup>[31]</sup> was used, allowing for an

unambiguous assignment to the experimental frequencies, as compiled in Table 1. The eigenvectors characterizing the atomic displacement coordinates are listed in the Supporting Information A.

## 3. Results and Discussion

The main focus of the article is placed on the analysis of the phonon modes in the temperature range of the reorientation of the Fe spins. Briefly, we will also discuss the electronic continuum.

### 3.1. Phonons

Figure 2a,b shows, respectively, the  $A_{1g}$  and  $E_g$  Raman spectra at temperatures ranging from 4.2 to 320 K. We can identify four  $A_{1g}$  phonons and four out of the expected five  $E_g$  phonons. These phonons harden continuously with decreasing temperature. The absent fifth  $E_g$  phonon might be too weak in intensity to be detected.

For a quantitative analysis the phonon peaks were fitted using a Voigt function, which is a convolution of the Lorentzian shape of the phonons and a Gaussian for the spectral resolution of the setup. In the narrow spectral range displayed in Figure 2 and the laser line used, the resolution is constant and was set at  $2.8 \text{ cm}^{-1}$ . Thus the widths indicated directly correspond to those of the phonons. The reasonable quality of the fits (see Figure S1, Supporting Information) indicates that the Lorentzian widths  $\Gamma_L(T)$  result from the finite life time of the phonons, determined by phonon–phonon decay into two modes having the same energy  $\omega_0/2$  and opposite wave vectors  $k$  and  $-k$ .<sup>[32]</sup>

The peak energies and line widths (FWHM) derived in this way are shown in Figure 3 and 4, and labeled consecutively from low to high. Their respective values at 4.2 K are listed in Table 1 and found to be in good agreement with the simulation. All phonon modes become harder and narrower upon cooling. The usual changes in width and energy are related to the unharmonic decay<sup>[32]</sup> and the lattice contraction.<sup>[33]</sup> However, as opposed to the  $E_g$  modes some of the  $A_{1g}$  modes show weak but significant deviations from the expected behavior in the temperature range around 100 K. In particular, kinks are observed in the energies of modes 1, 3, and 4 (see hatched range in Figure 3a,c). After remeasuring the  $A_{1g}$  spectra (open symbols in Figure 3a–d) the kinks can still be observed but are shifted slightly. The origin of this shift is not entirely clear but may be related to the first-order

**Table 1.** Phonon energies and widths (FWHM) of  $\text{Fe}_3\text{Sn}_2$  at 4.2 K.  $\text{Fe}_3\text{Sn}_2$  has four fully symmetric and five  $E_g$  phonon modes, four of which were observed experimentally. In addition to the theoretical and experimental energies  $\omega_0$  and Lorentzian widths  $\Gamma_L(T)$  the table displays also the phonon–phonon coupling parameters  $\lambda_{i,\text{ph-ph}}$  as derived from the approximative harmonic fits to the temperature-dependent line widths. The two values of  $\lambda_{1,\text{ph-ph}}$  for  $A_{1g}(1)$  correspond to temperatures below and above 100 K, as shown in Figure 3a by dashed–dotted and dotted lines, respectively.

Phonon		$A_{1g}(1)$	$A_{1g}(2)$	$A_{1g}(3)$	$A_{1g}(4)$	$E_g(1)$	$E_g(2)$	$E_g(3)$	$E_g(4)$	$E_g(5)$
Energy ( $\text{cm}^{-1}$ )	Simulation	83.9	140.1	232.1	241.8	92.7	138.2	147.1	196.7	278.3
	Experiment	86.6	146.8	237.7	251.6	94.3	133.8	147.0	199.8	–
FWHM ( $\text{cm}^{-1}$ )		4.5	4.1	4.7	4.9	3.6	3.1	3.8	4.1	–
$\lambda_{i,\text{ph-ph}}$		0.20; 0.05	0.14	0.68	0.74	0.11	1.11	0.29	0.42	–

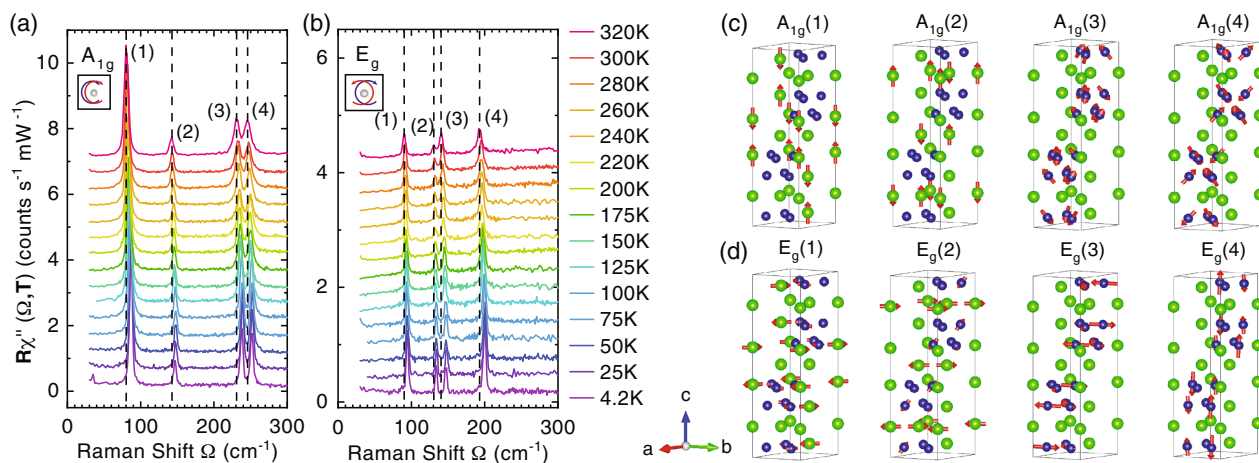


**Figure 2.** Raman spectra and phonon eigenvectors of  $\text{Fe}_3\text{Sn}_2$ . a,b) Temperature dependence of the eight observed phonon modes of  $\text{Fe}_3\text{Sn}_2$ . The spectra at the lowest temperature have the experimental intensity. The  $A_{1g}$  spectra are consecutively offset by  $0.5 \text{ cts s}^{-1} \text{ mW}^{-1}$  and those in  $E_g$  symmetry by  $0.3 \text{ cts s}^{-1} \text{ mW}^{-1}$  each for clarity. The clockwise and counterclockwise half-circle arrows indicate the  $R$  and  $L$  polarization in (a) and (b), respectively. Columns (a) and (b) separately display the  $A_{1g}$  and  $E_g$  phonon modes, respectively; c,d) the respective eigenvectors (small amplitudes omitted).

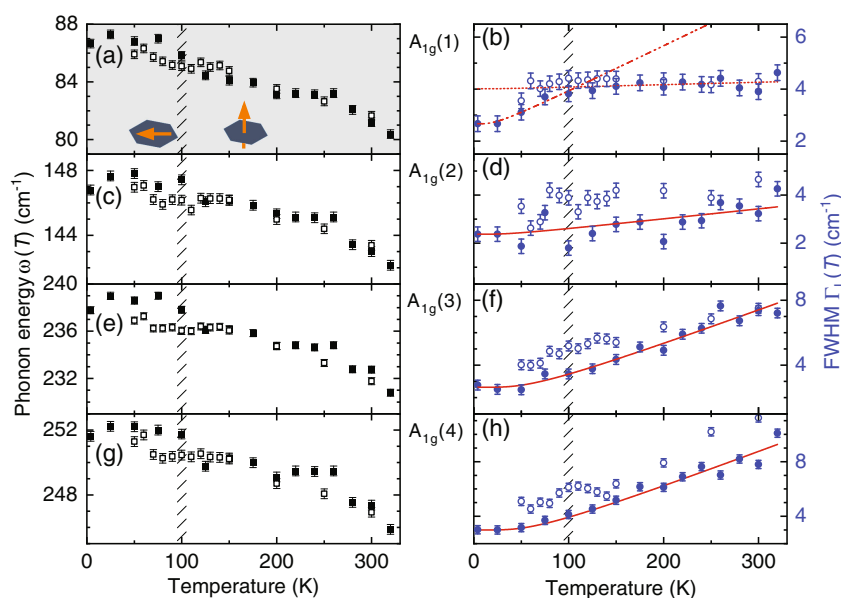


**Figure 3.** Phonon energies  $\omega_0$  (black) and Lorentzian widths  $\Gamma_L$  (blue) of  $\text{Fe}_3\text{Sn}_2$  in  $A_{1g}$  symmetry. The average magnetization with respect to the  $ab$  plane is indicated in (a). The parameters are derived by fitting procedures as described in the text. The first series of measurements (full black and blue symbols) were taken at temperatures listed in the following sequence: [320, 300, 200, 100, 75, 50, 25, 4.2, 125, 150, 175, 220, 240, 260, 280] K. The second series (open black and blue symbols) was measured in a row warming up from 50 K with an increment of 10 K in the interesting range. All line widths  $\Gamma_L$  were fitted according to Equation (4) (red lines). The linewidth of the  $A_{1g}$  mode at  $86 \text{ cm}^{-1}$  in (a) shows anomalous behavior, displaying a change in the expected temperature dependence at  $\approx 100 \text{ K}$  as indicated by the hatched area. Equation (4) yields  $\lambda_{\text{ph-ph}} = 0.2$  at low temperature and only 0.05 above 100 K.

nature of the reorientation transition and the then expected hysteresis.<sup>[34]</sup> In fact, the open points were obtained upon heating from low to high temperature in an uninterrupted series, whereas the black points were measured upon cooling as indicated in the figure caption. More experiments are required to finally clarify this issue.

The conventional reduction of the phonon widths with decreasing temperature can be understood in terms of the anharmonic decay described earlier<sup>[32]</sup> and may be represented by

$$\Gamma_L(T) = \Gamma_{L,0} \left( 1 + \frac{2\lambda_{\text{ph-ph}}}{\exp(\frac{\hbar\omega_0}{2k_B T}) - 1} \right). \quad (4)$$

$\Gamma_{L,0}(T)$  and  $\omega_0$  in Equation (4) can be extrapolated to zero from the experimental points below 50 K, leaving only the phonon–phonon coupling  $\lambda_{i,\text{ph-ph}}$  as a free parameter. The corresponding curves are displayed in red in Figure 3, 4, and the resulting values for  $\lambda_{\text{ph-ph}}$  are compiled in Table 1. As



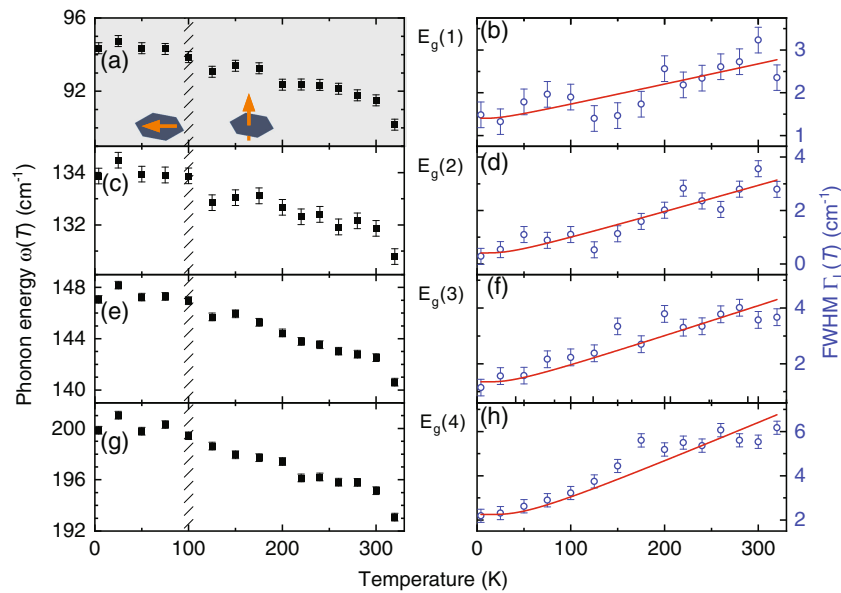


**Figure 4.** Phonon energies  $\omega_0$  (black) and Lorentzian widths  $\Gamma_L$  (blue) of  $\text{Fe}_3\text{Sn}_2$  in  $E_g$  symmetry. The linewidths and phonon energies behave like usual phonons without anomaly near the spin reorientation transition temperature.

opposed to the line width, the phonon energy depends on the occupation and the thermal expansion, where the latter is approximately larger by two orders of magnitude and depends crucially on the variation of the interatomic potential with distance.<sup>[33]</sup> The temperature dependences of the phonon width and energy are related by the usual Kramers–Kronig transformation and was determined for constant volume by Balkanski and co-workers.<sup>[35]</sup> In an experiment the pressure rather than the volume is constant, and this approach is not applicable (see, e.g., Eiter et al.<sup>[25]</sup>). Thus, the analysis of the phonon energy requires the thermal expansion and the Grüneisen parameters, which are currently not available.

All phonons except for one show essentially conventional behavior and become exponentially narrower upon cooling. Only the  $A_{1g}$  (1) phonon at  $86\text{ cm}^{-1}$  shows unexpected behavior directly in the data, and the description of the temperature dependence according to Equation (4) is similar to the other modes only for  $T \leq 100\text{ K}$  (dashed–dotted in Figure 3a) and yields  $\lambda_{1,\text{ph-ph}} = 0.2$ . For  $T \geq 100\text{ K}$  (dotted) the width is almost temperature independent, corresponding to an unusually small coupling of  $\lambda_{1,\text{ph-ph}} = 0.05$ . So we conclude that the symmetric phonon–phonon decay channel is essentially blocked when the spins point along the  $c$ -axis and becomes accessible only when the spins are rotated into the  $ab$  plane. This hand-waving argument certainly needs further theoretical analysis but a realistic model of the spin–phonon coupling is beyond the scope of this article and requires complex, presumably numerical work.

### 3.2. $E_g$ Continuum at Low Energy

Because  $\text{Fe}_3\text{Sn}_2$  is purely metallic and orders at  $T_C \approx 670\text{ K}$ , gaps or isolated electronic or magnetic modes are not immediately

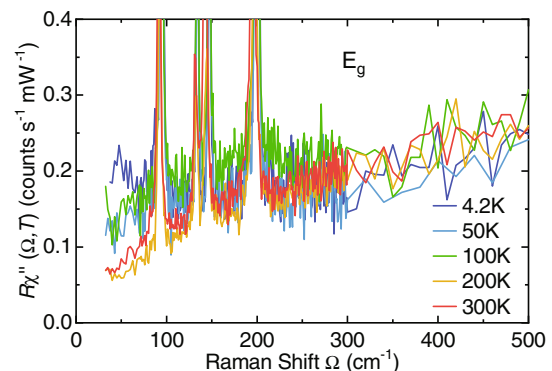


**Figure 5.** Electronic continuum in  $E_g$  symmetry at temperatures as indicated. The intensity below  $150\text{ cm}^{-1}$  increases continuously upon cooling, which implies a concomitant increase of the initial slope. The contribution from the laser line is negligible above  $30\text{ cm}^{-1}$ , indicating a metallic ground state that is consistent with the transport result. The increase at the limit  $\Omega \rightarrow 0$  is a real effect because the spectra at  $4.2\text{ K}$  have a peak at finite energy and then decrease again as opposed to a laser-induced divergence.

expected in the temperature range studied. Due to the magnetic anisotropy one may expect to see a single magnon at finite energy given by the anisotropy field. However, our microwave experiments show that the energy is presumably too small for the Raman experiment. In addition, fluctuations as a consequence of geometric frustration may smear out the energies.

The small variations with temperature of the  $E_g$  spectra below  $100\text{ cm}^{-1}$ , as shown in Figure 5, look unspectacular at first glance. However, the increase at low temperature must be considered real since a peak at  $\approx 47\text{ cm}^{-1}$  can be resolved at  $4.2\text{ K}$  rather than a divergence towards zero energy as in the case of diffuse scattering of the laser light. The intensity

increase may either originate from particle–hole excitations reflecting the temperature dependence of the resistivity (see Figure 1b) or from interband transitions as suggested by the optical conductivity<sup>[11]</sup> or from fluctuations similar to FeSe.<sup>[24]</sup> For clarification, larger crystals with flat surfaces are necessary.

Compared with the  $E_g$  spectra, the  $A_{1g}$  continuum is essentially temperature-independent (see Supporting Information C). As in the case of the  $E_g$  spectra, the data are reliable above  $30\text{ cm}^{-1}$ . Obviously, different excitations or regions of the Brillouin zone are projected in the two symmetries. Given the correspondence between transport and low-energy  $E_g$  spectra, the most likely explanation is that the carrier relaxation observed in the  $A_{1g}$  spectra is almost temperature-independent. This interesting anisotropy calls for more studies in optimized samples.

## 4. Conclusion

We have studied the Kagome ferromagnet  $\text{Fe}_3\text{Sn}_2$  using polarized Raman scattering. We identified all but one phonon lines and compared them to simulations of the lattice dynamics on the basis of density functional theory. The agreement between predicted and experimental phonon energies is better than 5 % for all lines. All phonons broaden upon heating. By assuming symmetric decay of the lines at  $\omega_0$  and  $|q| \approx 0$  into two lines at  $\omega_0/2$  and  $\pm k$  the dimensionless phonon–phonon coupling  $\lambda_{i,\text{ph-ph}}$  was extracted and found to be in the range 0.1–1.1 for all lines and temperatures with one exception: The  $A_{1g}$  phonon with the lowest energy exhibits  $\lambda_{1,\text{ph-ph}} = 0.2$  below 100 K and  $\lambda_{1,\text{ph-ph}} = 0.05$  above 100 K; thus, it has only very small phonon–phonon coupling at temperatures with the spins aligned along the  $c$ -axis parallel to the motion of the Sn atoms for the  $A_{1g}(1)$  mode. For this specific eigenvector, the coupling to the Fe spins parallel to the  $c$ -axis is certainly small, and one may speculate that the relatively large  $\lambda_{i,\text{ph-ph}}$  values of the other phonons result from coupling via the spins. As soon as the spins rotate into the plane also the  $A_{1g}(1)$  mode couples to the spins and thus participates in the anharmonic decay.

Because of the relatively high Curie temperature of  $T_C = 670\text{ K}$  in  $\text{Fe}_3\text{Sn}_2$  one does not expect strong changes in the electronic properties below room temperature. Yet, the  $E_g$  continuum exhibits a substantial variation with temperature at low energies, which is reminiscent of the strong temperature dependence of the resistivity  $\rho(T)$ . However, the low-energy peak in the  $E_g$  spectra may also originate from a bandgap induced by the spin reorientation as suggested by optical measurements,<sup>[11]</sup> although the rather different energies in the two experiments argue against this possibility, or from magnetic fluctuations in a geometrically frustrated system. There are no indications of a flat band in the 200 meV range. Yet, with the available equipment we cannot obtain sufficiently high data quality for a quantitative analysis.

## Supporting Information

Supporting Information is available from the Wiley Online Library or from the author.

## Acknowledgements

G.H. and L.P. contributed equally to the Raman study. The authors thank Y.-F. Xu for fruitful discussions. This work was supported by the Deutsche Forschungsgemeinschaft (DFG) through the coordinated programme TRR80 (Project-ID 107745057) and project HA 2071/12-1. G.H. would like to thank the Alexander von Humboldt Foundation for support through a fellowship. After submission the authors became aware of an earlier magnetization and magnetic force magnetometry study by Heritage et al.<sup>[36]</sup>

Open access funding enabled and organized by Projekt DEAL.

## Conflict of Interest

The authors declare no conflict of interest.

## Data Availability Statement

The data that support the findings of this study are available from the corresponding author upon reasonable request.

## Keywords

light scattering, magnetism, phonons

Received: April 21, 2021

Revised: July 28, 2021

Published online: September 12, 2021

- [1] G. Trumphy, E. Both, C. Djéga-Mariadassou, P. Lecocq, *Phys. Rev. B* **1970**, 2, 3477.
- [2] G. Le Caër, B. Malaman, B. Roques, *J. Phys. F: Met. Phys.* **1978**, 8, 323.
- [3] B. Malaman, C. Fruchart, G. Le Caër, *J. Phys. F: Met. Phys.* **1978**, 8, 2389.
- [4] L. A. Fenner, A. A. Dee, A. S. Wills, *J. Phys.: Condens. Matter* **2009**, 21, 452202.
- [5] Z. Hou, W. Ren, B. Ding, G. Xu, Y. Wang, B. Yang, Q. Zhang, Y. Zhang, E. Liu, F. Xu, W. Wang, G. Wu, X. Zhang, B. Shen, Z. Zhang, *Adv. Mater.* **2017**, 29, 1701144.
- [6] Z. Hou, Q. Zhang, G. Xu, C. Gong, B. Ding, Y. Wang, H. Li, E. Liu, F. Xu, H. Zhang, Y. Yao, G. Wu, X.-X. Zhang, W. Wang, *Nano Lett.* **2018**, 18, 1274.
- [7] J. Tang, Y. Wu, L. Kong, W. Wang, Y. Chen, Y. Wang, Y. Soh, Y. Xiong, M. Tian, H. Du, *Natl. Sci. Rev.* **2020**, 8, nwaa200.
- [8] J. Tang, L. Kong, Y. Wu, W. Wang, Y. Chen, Y. Wang, J. Li, Y. Soh, Y. Xiong, M. Tian, H. Du, *ACS Nano* **2020**, 14, 10986.
- [9] J.-X. Yin, S. S. Zhang, H. Li, K. Jiang, G. Chang, B. Zhang, B. Lian, C. Xiang, I. Belopolski, H. Zheng, T. A. Cochran, S.-Y. Xu, G. Bian, K. Liu, T.-R. Chang, H. Lin, Z.-Y. Lu, Z. Wang, S. Jia, W. Wang, M. Z. Hasan, *Nature* **2018**, 562, 91.
- [10] Q. Wang, S. Sun, X. Zhang, F. Pang, H. Lei, *Phys. Rev. B* **2016**, 94, 075135.
- [11] A. Biswas, O. Iakutkina, Q. Wang, H. C. Lei, M. Dressel, E. Uykur, *Phys. Rev. Lett.* **2020**, 125, 076403.
- [12] Z.-Z. Lin, X. Chen, *Phys. Status Solidi RRL* **2020**, 14, 1900705.
- [13] Z. Lin, J.-H. Choi, Q. Zhang, W. Qin, S. Yi, P. Wang, L. Li, Y. Wang, H. Zhang, Z. Sun, L. Wei, S. Zhang, T. Guo, Q. Lu, J.-H. Cho, C. Zeng, Z. Zhang, *Phys. Rev. Lett.* **2018**, 121, 096401.
- [14] N. Nagaosa, J. Sinova, S. Onoda, A. H. MacDonald, N. P. Ong, *Rev. Mod. Phys.* **2010**, 82, 1539.

- [15] C. Franz, F. Freimuth, A. Bauer, R. Ritz, C. Schnarr, C. Duvinage, T. Adams, S. Blügel, A. Rosch, Y. Mokrousov, C. Pfleiderer, *Phys. Rev. Lett.* **2014**, 112, 186601.
- [16] A. Mielke, *J. Phys. A* **1991**, 24, 3311.
- [17] A. Mielke, *J. Phys. A* **1991**, 24, L73.
- [18] A. Mielke, *J. Phys. A* **1992**, 25, 4335.
- [19] Y. Nagaoka, *Phys. Rev.* **1966**, 147, 392.
- [20] F. Pollmann, P. Fulde, K. Shtengel, *Phys. Rev. Lett.* **2008**, 100, 136404.
- [21] Z. P. Yin, K. Haule, G. Kotliar, *Nat. Mater.* **2011**, 10, 932.
- [22] I. Leonov, S. L. Skornyakov, V. I. Anisimov, D. Vollhardt, *Phys. Rev. Lett.* **2015**, 115, 106402.
- [23] K. M. Stadler, Z. P. Yin, J. von Delft, G. Kotliar, A. Weichselbaum, *Phys. Rev. Lett.* **2015**, 115, 136401.
- [24] A. Baum, H. N. Ruiz, N. Lazarević, Y. Wang, T. Böhm, R. Hosseinian Ahangharnejhad, P. Adelman, T. Wolf, Z. V. Popović, B. Moritz, T. P. Devereaux, R. Hackl, *Commun. Phys.* **2019**, 2, 14.
- [25] H.-M. Eiter, P. Jaschke, R. Hackl, A. Bauer, M. Gangl, C. Pfleiderer, *Phys. Rev. B* **2014**, 90, 024411.
- [26] G. Kresse, J. Hafner, *Phys. Rev. B* **1994**, 49, 14251.
- [27] G. Kresse, J. Furthmüller, *Comput. Mater. Sci.* **1996**, 6, 15.
- [28] G. Kresse, J. Furthmüller, *Phys. Rev. B* **1996**, 54, 11169.
- [29] G. Kresse, D. Joubert, *Phys. Rev. B* **1999**, 59, 1758.
- [30] J. P. Perdew, K. Burke, M. Ernzerhof, *Phys. Rev. Lett.* **1996**, 77, 3865.
- [31] A. Togo, I. Tanaka, *Scr. Mater.* **2015**, 108, 1.
- [32] P. G. Klemens, *Phys. Rev.* **1966**, 148, 845.
- [33] C. Postmus, J. R. Ferraro, S. S. Mitra, *Phys. Rev.* **1968**, 174, 983.
- [34] N. Kumar, Y. Soh, Y. Wang, Y. Xiong, *Phys. Rev. B* **2019**, 100, 214420.
- [35] M. Balkanski, R. F. Wallis, E. Haro, *Phys. Rev. B* **1983**, 28, 1928.
- [36] K. Heritage, B. Bryant, L. A. Fenner, A. S. Wills, G. Aeppli, Y.-A. Soh, *Adv. Funct. Mater.* **2020**, 30, 1909163.